AIAA JOURNAL
Vol. 50, No. 10, October 2012

Transition Experiments on Slightly Blunted Cones with Distributed Roughness in Hypersonic Flight

Daniel C. Reda* and Michael C. Wilder†
NASA Ames Research Center, Moffett Field, California 94035-1000
and
Dinesh K. Prabhu‡
ERC, Inc., Moffett Field, California 94035-1000

DOI: 10.2514/1.J051616

Slightly blunted cones with smooth tips and roughened frusta were flown in the NASA Ames Research Center hypersonic ballistic range through quiescent air environments at a Mach number of 10. Global surface-temperature distributions were optically measured and analyzed to determine the transition onset location on the roughened surface of each model. A series of tests was conducted over a range of freestream pressures, from which the progression of the transition front over the roughened surface was determined as a function of freestream pressure. Real-gas Navier–Stokes calculations of the laminar boundary layer were conducted at the measured flight Mach number and wall temperature at the transition onset location for each shot, and results used to predict key dimensionless parameters required to correlate transition on such configurations in hypersonic flow. For distributed roughness elements totally immersed within the laminar boundary layer, the critical-roughness-Reynolds-number correlating approach was found to well model transition onset and progression over the roughened conic frusta. The critical value of the roughness Reynolds number for transition was found to be 266 ± 20%, in agreement with the critical value of 250 ± 20% determined in earlier experiments for transition on rough blunt bodies in hypersonic free flight.

Nomenclature

D_B	=	model base diameter
h	=	local surface elevation of roughness
k	=	three-dimensional roughness-element height
$\bar{k}$	=	average roughness-element height for distributed roughness
k_{mp}	=	most probable roughness-element height
L	=	model length
M	=	Mach number
P	=	static pressure
Re_D	=	freestream Reynolds number, $\frac{\rho_\infty V_\infty D_B}{\mu_\infty}$
Re_{kk}	=	roughness Reynolds number, $\frac{\rho_k u_k \bar{k}}{\mu_w}$
R_N	=	model nose-tip radius
T	=	temperature
TH	=	temperature threshold
TR	=	transition
u	=	fluid velocity component parallel to the wall
V	=	model velocity
X	=	model axial length measured from tip along centerline
x, y, z	=	local surface coordinates used in surface-roughness characterization
δ	=	boundary-layer thickness
θ	=	boundary-layer momentum thickness
θ_c	=	cone frusta half-angle
μ	=	fluid viscosity
ρ	=	fluid density
σ	=	standard deviation
φ	=	flow-aligned polar coordinate on hemisphere surface measured from stagnation point

Subscripts

k	=	based on conditions in the laminar boundary layer at the roughness height
TR	=	at transition location
w	=	based on wall conditions
∞	=	freestream

Presented at the 41st AIAA Fluid Dynamics Conference, Honolulu, HW, June 27–30, 2011; received 13 September 2011; revision received 28 March 2012; accepted for publication 29 March 2012.

*Senior Research Scientist, Aerothermodynamics Branch, MS 230-2. Fellow AIAA.
†Senior Research Scientist, Aerothermodynamics Branch, MS 230-2. Associate Fellow AIAA.
‡Senior Research Scientist. Associate Fellow AIAA.

I. Introduction

BOUNDARY-layer transition, aside from being one of the most challenging problems of basic fluid physics, remains a real-world problem to designers of advanced flight systems. Accurate predictions of viscous flowfields around high-speed aircraft, missiles, and entry vehicles are of paramount importance to each system's design and subsequent flight performance. Boundary-layer transition is known to affect vehicle dynamics, drag, and surface heat transfer significantly.

In the hypersonic flow regime, thermal protection of flight vehicles is most often accomplished with ablating heat shields. In such cases, frictional energy generated between the flight vehicle and its atmospheric environment is absorbed and shed as the thermal protection system (TPS) ablates and recedes.

Ablating TPS materials on planetary entry trajectories first experience thermochemistry under high-altitude, low-Reynolds-number conditions. Such laminar-flow ablation causes the formation of a distributed surface microroughness pattern characteristic of the TPS material composition and fabrication process [1,2]. Once formed, these distributed surface-roughness elements create disturbances within the laminar boundary layer flowing over the surface. As altitude decreases, Reynolds number increases and flowfield conditions capable of amplifying these roughness-induced perturbations may eventually be achieved. Whether or not these roughness-induced disturbances cause a breakdown to turbulence is a critical design issue [2]. Boundary-layer transition to turbulence

results in more severe heat transfer rates and accelerated surface recession. Ablating TPS thus can potentially encounter failure mechanisms associated with exceeding bond-line temperature limits, burn through, or thermostructural breakup.

Early manned entry vehicles were blunt capsules with ablating TPS in the shape of a sphere segment. Unmanned planetary entry vehicles are generally axisymmetric in shape: slightly blunted slender cones for strategic applications and large bluntness, large-angle cones for planetary-exploration applications. Complicating the designs of such vehicles, the nose tips or nose caps are often composed of ablative materials different from those deployed on the conic afterbodies.

Early transition research on smooth and rough bodies at hypersonic speeds was conducted in conventional hypersonic wind tunnels. However, it soon became apparent that transition physics was adversely affected by facility noise, both convected along the freestream from plenum chambers and radiated into the freestream from turbulent boundary layers on the nozzle walls. The evolution of this understanding is covered in [3–9]. A coordinated national effort to overcome these testing limitations was put forward by Reshotko [10], involving the development and use of quiet supersonic and hypersonic wind tunnels, supplemented by experiments in quiet ballistic ranges and in atmospheric flight tests. A recent review on this subject is given by Schneider [11].

Results of ballistic-range transition experiments using smooth-wall conical models launched at supersonic and hypersonic speeds were reported by Sheetz [12–14], Potter [15,16], and Reda [17]. The effects of distributed roughness on blunt-body transition at hypersonic speeds were investigated in the ballistic-range experiments of Reda [1,2], Reda and Raper [18], and Reda et al. [19]. Most recently, the effects of isolated roughness elements on blunt-body transition in hypersonic free flight were reported [20].

A review of roughness-dominated transition correlations for reentry applications was given by Reda [21]. Based on analyses of published correlations for blunt bodies, attachment lines, and windward surfaces of lifting entry vehicles, it was found that all of these transition correlations could be recast into and be well modeled by the critical-roughness-Reynolds-number concept. This concept is attributed to Schiller [22], who hypothesized that, at some critical value, vortices would be shed from the top of the roughness element (s), causing an abrupt breakdown to turbulence. The critical Reynolds number was based on smooth-wall laminar boundary-layer conditions at the roughness height, and the length scale was the roughness height. This modeling approach was further corroborated by analyses of roughness-dominated transition databases obtained since this 2002 review [19,20].

It is acknowledged that the assumed breakdown mechanism stated is simplistic and poorly understood. Both Reshotko and Tumin [23] and Schneider [24] have presented detailed discussions of potential breakdown mechanisms associated with surface roughness. However, a validated computational capability to predict roughness-dominated transition from first principles does not yet exist. Until such a predictive capability becomes available, the critical-roughness-Reynolds-number approach offers a semi-empirical methodology to designers of hypersonic flight vehicles.

Transition onset and progression over blunt (hemispherical) shapes with distributed surface-roughness patterns induced by laminar ablation processes are well modeled by the critical-roughness-Reynolds-number approach [19]. Figure 1 illustrates the sequence of events that occur on a typical hypersonic planetary entry trajectory. For the results presented in [19], real-gas Navier–Stokes computations were used to predict the distribution of the roughness Reynolds number Re_{kk} around the hemispherical shape at each of several freestream pressures. The numerics and models employed in the codes are described in detail in the references cited in the next section. The critical value of 250 is first achieved at the sonic point, and, as the freestream pressure increases (altitude decreases), the intersection of the predicted Re_{kk} distribution with the critical value systematically moves forward toward the stagnation point.

What is unknown, at this point, is whether or not the critical-roughness-Reynolds-number correlating approach can be applied with confidence to the frusta of blunted cones with distributed roughness, in which boundary-layer edge conditions are supersonic. The present paper addresses this issue.

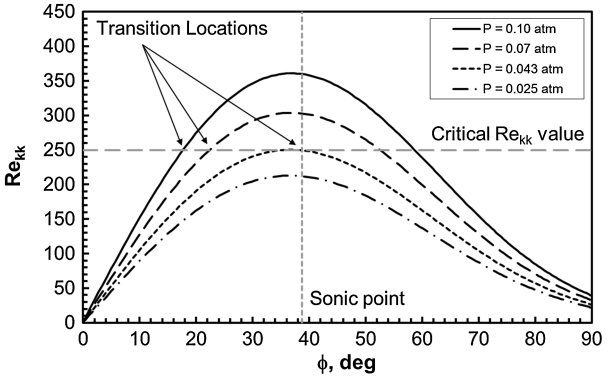

Fig. 1 Transition onset and progression on hemispherical shapes with distributed roughness. $M_\infty = 12$; $R_N = 14.3$ mm; $\bar{k} = 15.2$ μm; gas = air; $T_w = 900$ K.

II. Pretest Computations

As with the roughened nose-tip experiments discussed in [19] and Fig. 1, real-gas Navier–Stokes computations were used to predict roughness-Reynolds-number distributions over blunt conic bodies with smooth nose tips and roughened frusta. The idea of roughening only the conic frustum was to ensure a known laminar boundary-layer profile entering the roughened region, thus isolating the frustum transition problem from the nose-tip transition problem. Axisymmetric laminar-flow computations were performed using v4.02.2 of the computational fluid dynamics (CFD) code DPLR (data-parallel line relaxation) [25,26]. A five-species (N_2, O_2, NO, N, O) model was employed for air. In all computations, thermal equilibrium was assumed, and thermodynamic properties (enthalpy and specific heat) of constituent species were determined using curve fits [27]. All pretest cases were computed with a prescribed wall temperature, equal to the wall temperature assumed to exist upstream of transition onset. Posttest computations used the measured wall temperature upstream of transition onset. The wall was assumed to be fully catalytic to recombination of atomic species.

A slightly blunted cone of half-angle $\theta_c = 30$ deg, at a nominal freestream velocity of 3.4 km/s ($M_\infty = 10$) in air, was selected for investigation. These conditions would ensure an aerodynamically stable shape with a supersonic edge Mach number. Sample results are shown in Fig. 2 for the chosen nose-tip radius $R_N = 0.045$ in. (1.14 mm) and an average surface-roughness height $\bar{k} = 0.00022$ in. (5.6 μm) beginning at $X/L = 0.2$ and extending from there to the base of the cone. The critical value of Re_{kk} was unknown a priori, and so a value of 250 was chosen as a pretest estimate.

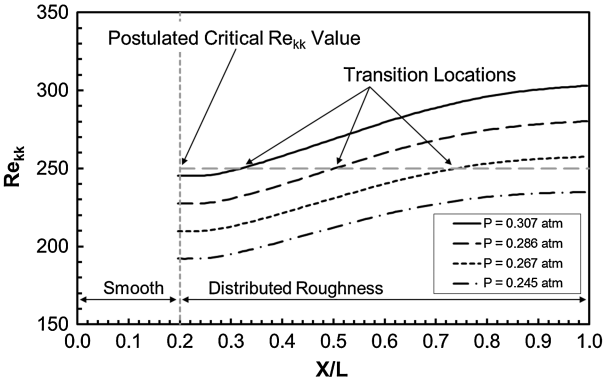

Fig. 2 Transition onset and progression on frusta of small-bluntness cones with distributed roughness. $M_\infty = 10$; $R_N = 1.143$ mm; half-angle = 30 deg; $\bar{k} = 5.6$ μm; gas = air; $T_w = 650$ K.

As can be seen, for a small-bluntness tip, Re_{kk} values increase with increasing distance along the roughened frustum, reaching a maximum value at the base of the cone. If a critical value for Re_{kk} exists, transition onset would first be achieved at the cone base. Systematic increases in freestream pressure (reductions in effective altitude) would then cause the predicted crossing of the computed Re_{kk} distribution with the critical Re_{kk} value to progress forward toward the upstream-most location of the distributed roughness pattern. This trend, if substantiated by experiment, would be similar to that encountered for hypersonic flow over blunt, roughened hemispheres.

III. Ballistic-Range Models

The model geometry was chosen for its aerodynamic stability and, based on pretest Navier–Stokes computations, the expected laminar boundary-layer characteristics at achievable test conditions. The geometric parameters were $\theta_c = 30$ deg; $R_N = 0.045$ in. (1.14 mm), smooth; $D_B = 1.191$ in. (30.25 mm); and $L = 0.994$ in. (25.25 mm), with frustum roughness beginning at $X/L = 0.2$. Both titanium (6Al-4V) and stainless-steel (304) alloys were used in model fabrication. Simple one-dimensional thermal analyses were performed to determine the range of test conditions that would not cause melting or ignition [28] of the nose tips. Thermophysical properties of the alloys used were obtained from [29,30], and stagnation-point heating rates were from the pretest CFD. Predicted and measured stagnation-point surface temperatures were always well below the maximum-use temperatures for both metals. Surface-roughness distributions were created by bead-blasting methods described in the next section. For the roughened titanium models, the mean roughness height was $\bar{k} = 12.3$ μm, and the mean roughness heights relative to the momentum thickness and boundary-layer thickness at $X/L = 0.2$ were $0.95 \leq \bar{k}/\theta \leq 1.18$ and $0.15 \leq \bar{k}/\delta \leq 0.20$, respectively, for 0.074 atm $\leq P_\infty \leq$ 0.15 atm. For the roughened steel models, the mean roughness height was $\bar{k} = 5.6$ μm, and the mean roughness heights relative to the momentum thickness and boundary-layer thickness at $X/L = 0.2$ were $0.53 \leq \bar{k}/\theta \leq 0.71$ and $0.09 \leq \bar{k}/\delta \leq 0.12$, respectively, for 0.141 atm $\leq P_\infty \leq$ 0.307 atm.

Figure 3a shows a photograph of a typical model, mounted in the launch sabot with one-half of the sabot removed to reveal the full length of the model. Figure 3b shows a shadowgraph of this model in flight at $M_\infty = 10$.

IV. Surface Roughness

Model frusta were roughened using bead-blasting methodologies. Experimentation revealed that irregularly shaped, sharp-edged particles, such as aluminum oxide, were required to sufficiently roughen the metallic surfaces. Such particles both erode the surface and lift up material, resulting in a surface with elevations both higher and lower than the original smooth surface. Titanium was initially selected for the models for its low thermal conductivity [29], which provides for a more rapid increase in surface temperature during flight. For the $M_\infty = 10$ test condition, however, freestream pressure was limited to no more than 0.2 atm to prevent combustion [28] of the titanium nose tip. To achieve roughness Reynolds numbers near the postulated critical value at these freestream pressures, a surface roughness of 10–15 μm was required. Subsequent experiments were conducted using stainless-steel models, which could be flown at higher freestream pressures (the surface did not heat as rapidly because of the higher conductivity of this alloy [30] compared with Ti-6Al-4V), and required smaller surface-roughness heights to achieve similar roughness Reynolds numbers. The titanium frusta were roughened by impacting with 60-grit aluminum-oxide particles (nominal particle size 250 μm). The stainless-steel models were impacted with 120-grit aluminum-oxide particles (nominal particle size 106 μm), and then bead blasted a second time with regularly shaped ceramic microspheres (also 120 grit). This two-sequence approach removed many of the largest-height roughness elements, yielding a more uniform (smaller) height distribution.

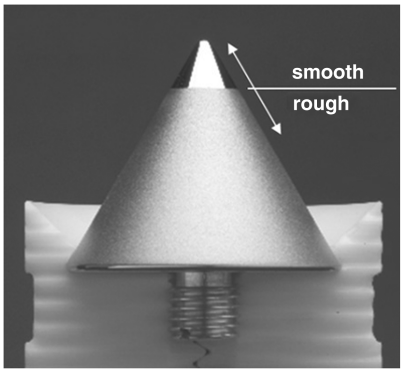

a)

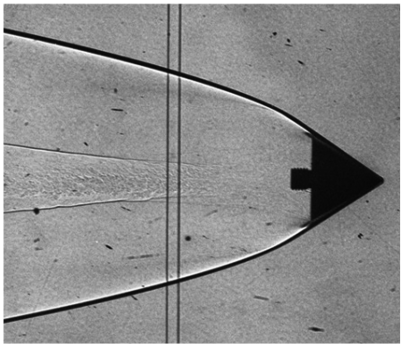

b)

Fig. 3 a) Model mounted in launch sabot with two of four sabot fingers removed; b) model in flight at $M_\infty = 10$.

Resultant surface-roughness patterns were measured by reflected white light interferometry [31]. The quoted resolution and accuracy of the instrument were 12 and 60 nm, respectively. Measurements were made over surface areas ranging from 1×1 mm up to 4×6 mm, at a sampling step size of 1 μm in both x and y. Figures 4a and 4b show representative measured surface elevations over a small surface area for each bead-blasting procedure. Similar measurements were made on multiple roughened surfaces and at multiple areas on each surface.

As can be seen in Fig. 4, the surface roughness consists of a fine-scale, high-wave-number (short wavelength) surface height fluctuation superimposed on a field of larger-scale structures. These larger-scale structures were considered to be the characteristic roughness elements, and the surface roughness was characterized by the average height $\bar{k}$ of these roughness elements. A topographical analysis was performed on the measured surface elevation maps to identify individual roughness elements. One such roughness element identified in the data set shown in Fig. 4b is shown, and enlarged in Fig. 4c. Measured height profiles, one profile taken through the center of the roughness element and a second taken alongside the roughness element, are shown in Fig. 4d to illustrate the short-wavelength height fluctuations that are not associated with characterizing a roughness element. Figure 5 shows measured roughness elevations on a stainless-steel model taken on multiple axial cut planes; smooth-to-rough transition occurs at $X/L = 0.2$. A single profile through the roughness distribution is unlikely to pass through the peak of many roughness elements, as illustrated in Fig. 4, and so will generally show heights lower than the mean roughness-element height. The resultant roughness-element-height distributions for the two cases shown in Fig. 4 are presented in Fig. 6. The roughness-element-height distribution on the titanium is clearly less uniform than on the steel models, with a longer tail of less-frequently occurring, large-height roughness elements.

Roughness-element heights were measured relative to the unimpacted (smooth) surface elevation. Surface depressions below the smooth-wall reference were not included in the determinations of the roughness distributions shown in Fig. 6. Depressions below the

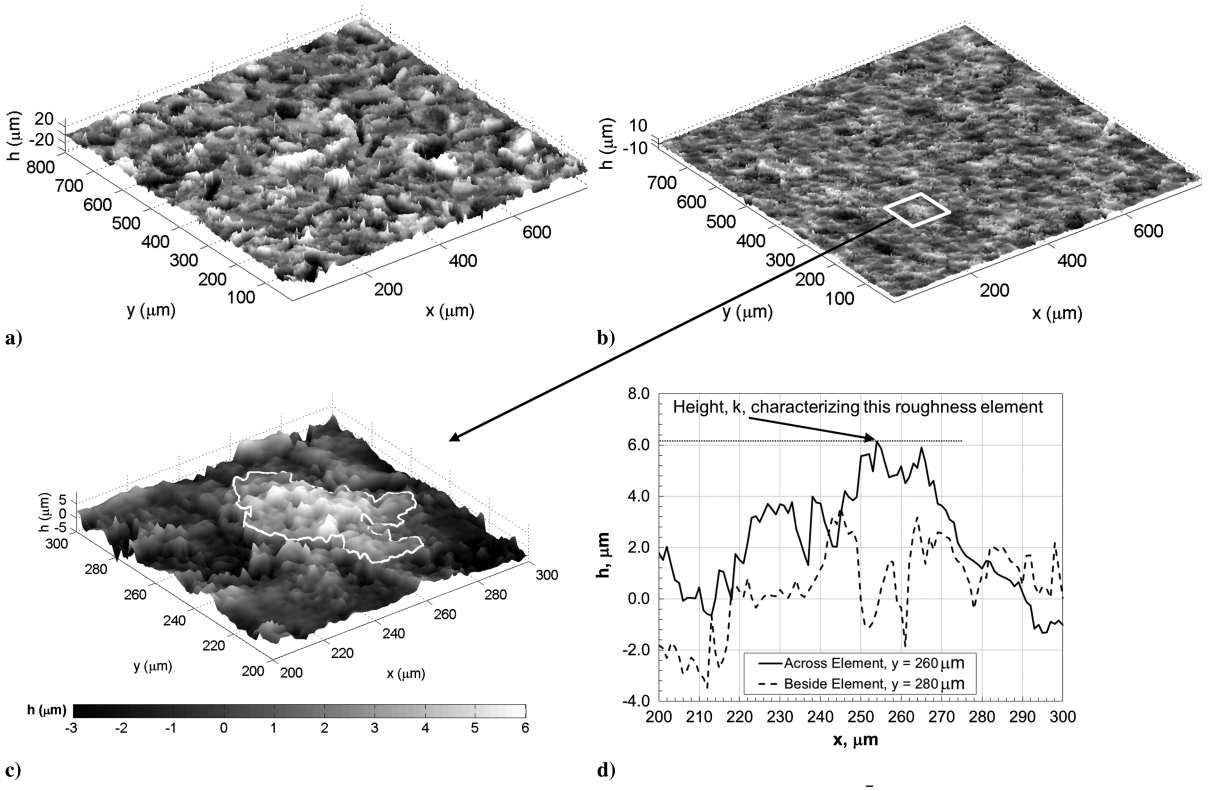

Fig. 4 Measured surface elevations: a) single bead-blasting procedure applied to titanium models, $\bar{k} = 12.3\ \mu$m; b) two-sequence bead-blasting procedure applied to stainless-steel models, $\bar{k} = 5.6\ \mu$m; c) individual roughness element; and d) surface height profiles through and beside the roughness element.

initial smooth-wall surface were reasoned to be stagnant fluid zones, since the incoming laminar boundary layer developed over the smooth-wall surface. This is in contrast to the roughness height definition for the laminar-ablated nose-tip problem [19], wherein the distributed roughness extends to the stagnation point, hence no smooth surface exists upstream of the roughness.

V. Experimental Approach

The experiments were performed in the Hypervelocity Free-Flight Aerodynamic Facility at NASA Ames Research Center. The ballistic range, shown in Fig. 7, employs a two-stage light-gas gun to launch individual models on trajectories through a quiescent, controlled-atmosphere test section. The gun used has an inner diameter of 38.1 mm (1.5 in.), and the test section is 1 m across at midrange and 23 m long, measured from the first optical measurement station to the last. The models are in flight for an additional 10 m from the exit of the gun barrel to the first optical measurement station, during which time the launch sabot is separated from the model by aerodynamic forces and trapped in the separation tank. There are 16 optical measurement stations, spaced 1.524 m (5 ft) apart, along the length of the test section. Each station is equipped with orthogonal-viewing parallel-light shadowgraph cameras and high-speed timers for recording the flight trajectories. Pitch and yaw angles were measured from orthogonal-view shadowgraphs taken at multiple stations along each range trajectory. For the shots reported here, the maximum total angle of attack was less than 1.6 deg, and the models executed 1 to 1.5 oscillation cycles, depending on freestream pressure, between launch and the last measurement station.

Models described in Sec. III were launched without spin at a nominal velocity of 3.4 km/s (11, 150 ft/s) into quiescent room temperature air, yielding a freestream Mach number of 10 and an edge Mach number between 2.1 and 2.6 at the beginning of the roughness, reaching Mach 3.5 asymptotically at $X/L \sim 0.8$, for the freestream pressures of these tests. Freestream static pressure was systematically varied over the range $0.074\ \text{atm} \leq P_\infty \leq 0.307\ \text{atm}$ to vary the primary independent variable Re_{kk}.

For these experiments, three of the optical measurement stations were equipped with high-speed thermal imaging infrared (IR) cameras to record the instantaneous global surface intensity

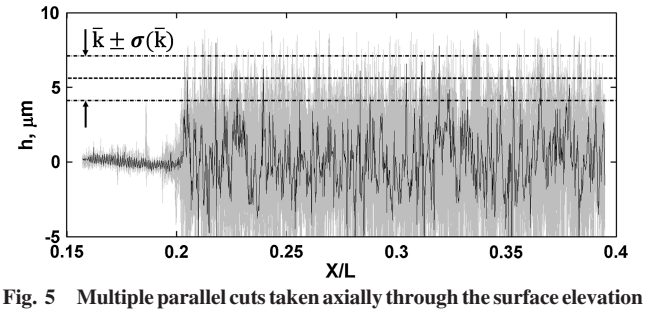

Fig. 5 Multiple parallel cuts taken axially through the surface elevation data set for a steel model.

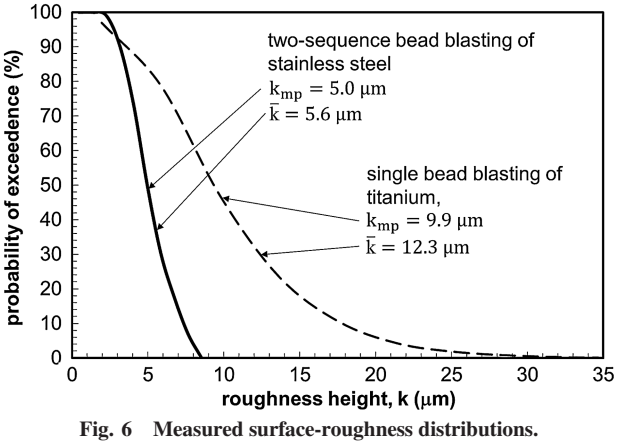

Fig. 6 Measured surface-roughness distributions.

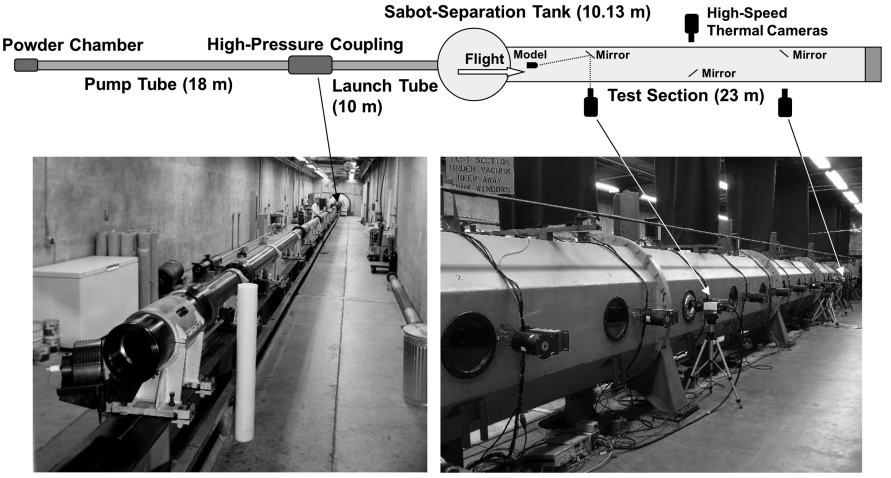

Fig. 7 The NASA Ames Research Center free-flight ballistic range.

distributions on the models: two cameras imaged one side of each model at the beginning and end of the range, respectively, while a third camera imaged the opposite side of each model at midrange. These IR cameras were sensitive to the 3–5 μm IR wavelength band. All images were recorded with a 1 μs exposure time, and exposure level was controlled with neutral density filters having optical densities ranging from 0 to 1. The minimum detectable temperature was typically between 400 and 500 K, depending on the filter selection.

The cameras were located outside the test section, and used first-surface aluminum plane mirrors placed inside the test section, just off the line of flight (as illustrated in Fig. 7), to view the models. An example image is shown in Fig. 8a. The models were imaged from an angle between 20 and 25 deg off the nominal flight line, or as nearly head on as possible, using a telephoto lens from a long distance relative to the model dimensions. As a consequence, only the component of motion normal to the image plane significantly contributed to motion blur. The motion normal to the image plane in 1 μs was between 4 and 6% of the model length, or approximately 2 pixels. The standard deviation in the transition-front location, when averaged circumferentially around a model, was between 1 and 7% of the model length.

The shock-layer gases of the bow shock radiate slightly in the IR wavelengths for the conditions of these experiments and have the potential to bias the surface-temperature measurements. A localized plume of helium was created to temporarily quench this gas-cap radiation at each imaging station, as discussed in [32]. The model was in the helium less than 0.5% of the total flight time, thus its effect on the integrated convective heating over the entire trajectory was minimal.

Camera calibration procedures outlined in [32,33] were employed to convert intensity images to global surface-temperature images (see Fig. 8b). The response of each camera was calibrated against a blackbody radiation standard by imaging the blackbody source on an optical path equivalent to that employed in the ballistic-range tests. The standard deviation of temperature measurements of the calibration source was less than 5 K, for both spatial and temporal variations.

Transition-front locations were determined by identifying the axial locations where the measured wall temperature rose above, and stayed above, the smooth-wall temperature at the start of the roughness. This is illustrated in Fig. 9 for a representative axial temperature profile obtained in one test of this series.

Oblique views of the left and right sides of the model acquired at sequential stations were mapped to a single surface grid to determine a composite transition front around the model surface. Figure 10

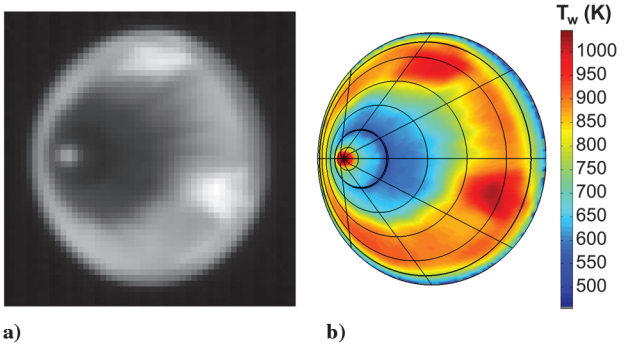

Fig. 8 Oblique view of a stainless-steel model, $M_\infty = 10$, $P_\infty = 0.225$ atm: a) IR image; b) surface-temperature distribution.

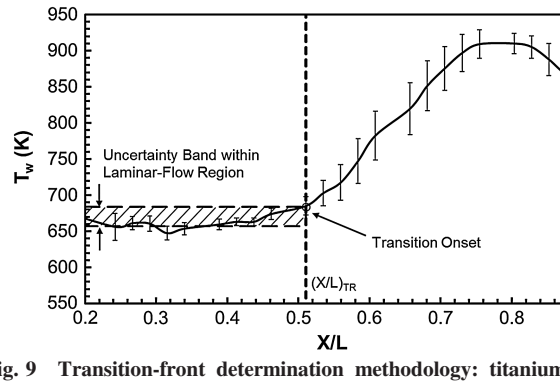

Fig. 9 Transition-front determination methodology: titanium cone, $M_\infty = 10$, $P_\infty = 0.132$ atm.

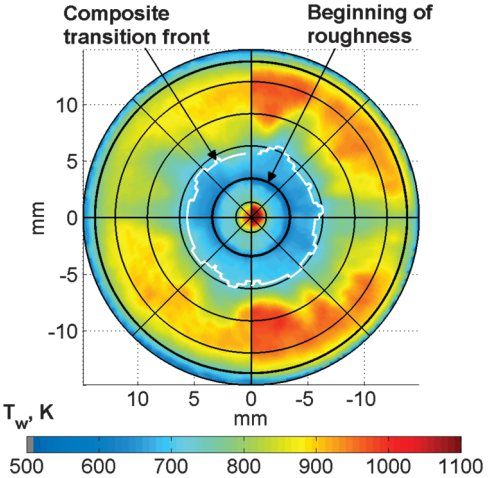

Fig. 10 Composite of two oblique-view IR images mapped to a common surface grid, titanium cone, $M_\infty = 10$, $P_\infty = 0.141$ atm.

shows an example composite image and transition front. The left side of this composite is cooler than the right because that image was acquired earlier in the flight; however, the transition front is continuous. Arithmetic average transition-front locations taken from such composite transition-front distributions were then used to correlate the transition onset and progression results shown in the subsequent section.

VI. Results

Transition-front forward progression as a function of freestream static pressure is summarized in Figs. 11 and 12. For the roughened titanium frusta (Fig. 11), the transition front first occurred near the base of the cone and progressed forward with increasing freestream static pressure (freestream Reynolds number). No transition front was observed on an all-smooth model (not shown). Consistent with the wide range of surface-roughness-element heights measured on the titanium models (single bead-blasting procedure of Fig. 5), the observed transition fronts were initially ragged, as if formed by the merger of individual turbulent wedges emanating (presumably) from the highest peaks in the roughness distribution. As the transition front progressed forward, it became more uniform.

Similar trends were observed for the stainless-steel models (Fig. 12). In these cases, however, the more-uniform surface-roughness distribution created by the double-bead-blasting procedure (see again Fig. 5) yielded less circumferential variability

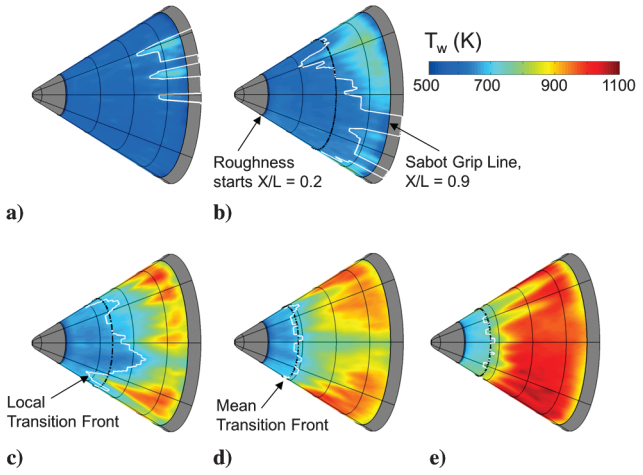

Fig. 11 Results for titanium cones with distributed surface roughness, $M_\infty = 10, \bar{k} = 12.3$ μm: a) $P_\infty = 0.074$ atm; b) 0.100 atm; c) 0.132 atm; d) 0.141 atm; e) 0.150 atm.

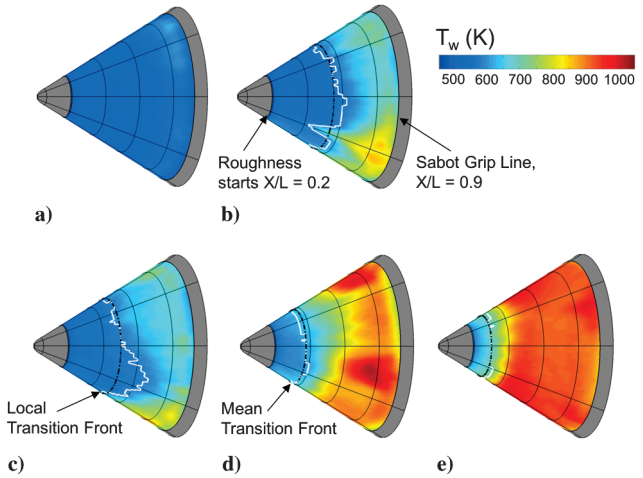

Fig. 12 Results for stainless-steel cones with distributed surface roughness, $M_\infty = 10$, $\bar{k} = 5.6$ μm: a) $P_\infty = 0.141$ atm; b) 0.184 atm; c) 0.225 atm; d) 0.266 atm; e) 0.307 atm.

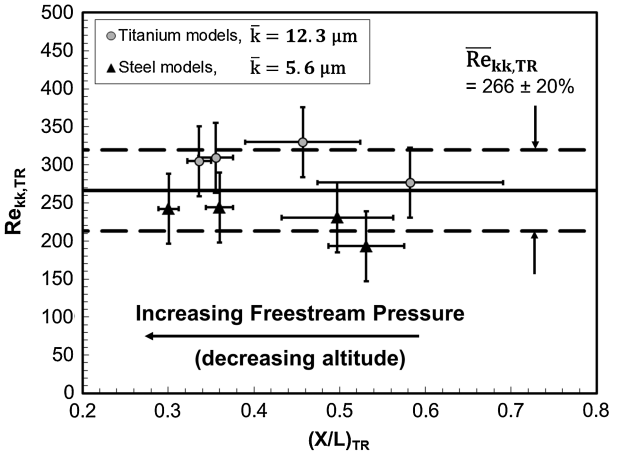

Fig. 13 Transition-front forward progression over roughened frusta.

in observed transition-front contours. Here also, the mean transition front was first observed near the cone base, progressing forward with increasing freestream static pressure (freestream Reynolds number).

Figure 13 presents combined results for both of the roughness distributions of Fig. 5. Critical roughness Reynolds number for transition is shown as a function of the average transition-front location along the roughened frusta. The horizontal error bars represent one standard deviation from the mean transition-front location for a given model (single shot), and indicate the uniformity of the transition fronts (compare the local transition fronts to the mean transition fronts in Figs. 11 and 12). The vertical error bars represent the standard deviation of mean $Re_{kk,TR}$ for all shots (steel and titanium) in this data set (eight shots). This value was used to capture the shot-to-shot variations in the correlation. For individual shots, the standard deviation of $Re_{kk,TR}$ around the local transition front was an order of magnitude lower (not shown). These results are slightly modified from those presented in the original meeting paper [34] in that posttest, as-measured trajectory, and surface-temperature distributions were employed in the final Navier–Stokes computations.

Observed transition-front progression over the roughened frusta occurred for an essentially constant value of the critical roughness Reynolds number, the average value of this correlating parameter being 266 ± 20%, in agreement with the critical value of 250 ± 20% determined for transition on rough blunt bodies in hypersonic free flight [19].

It can be seen in Fig. 13 that the critical roughness Reynolds numbers obtained on the titanium models fall above the average value, whereas those obtained on the steel models fall below the average value. This is attributed to the skewness differences in the roughness distributions formed on each material, as was discussed in Sec. IV. Reevaluating $Re_{kk,TR}$ at the most frequently occurring (most

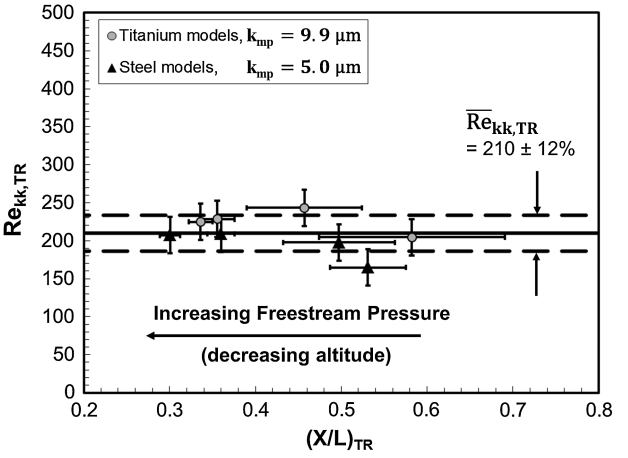

Fig. 14 Transition-front forward progression over roughened frusta.

probable) roughness-element height in each distribution, rather than the average height, results in an average critical roughness Reynolds number of $210 \pm 12\%$, with the titanium and steel model results in closer agreement with each other, as shown in Fig. 14.

VII. Conclusions

The critical-roughness-Reynolds-number correlating approach was found to well model transition onset and progression over roughened conic frusta of slightly blunted, smooth-tipped cones in hypersonic free flight. When using the average roughness-element height to characterize the roughness distribution, the critical value of the roughness Reynolds number for transition was found to be $266 \pm 20\%$. When using the most frequently occurring roughness-element height to characterize the roughness distribution, the critical value of the roughness Reynolds number for transition was found to be $210 \pm 12\%$. Both results are in agreement, within experimental uncertainty, with the critical value of $250 \pm 20\%$ determined in earlier experiments for transition on rough blunt bodies in hypersonic free flight.

Acknowledgments

This research was funded by the NASA Fundamental Aeronautics Program, Hypersonics Project, Deepak Bose, Associate Principal Investigator. Dinesh Prabhu is supported by contract NNA10DE12C from NASA Ames Research Center to ERC, Inc.

References

[1] Reda, D. C., "Comparative Transition Performance of Several Nosetip Materials as Defined by Ballistics-Range Testing," *Instrument Society of America Transactions*, Vol. 19, No. 1, 1980, pp. 83–98.

[2] Reda, D. C., "Correlation of Nosetip Boundary-Layer Transition Data Measured in Ballistics-Range Experiments," *AIAA Journal*, Vol. 19, No. 3, 1981, pp. 329–339. doi:10.2514/3.50952

[3] Pate, S. R., and Schueler, C. J., "Radiated Aerodynamic Noise Effects on Boundary-Layer Transition in Supersonic and Hypersonic Wind Tunnels," *AIAA Journal*, Vol. 7, No. 3, March 1969, pp. 450–457. doi:10.2514/3.5128

[4] Pate, S. R., "Supersonic Boundary-Layer Transition: Effects of Roughness and Freestream Disturbances," *AIAA Journal*, Vol. 9, No. 5, May 1971, pp. 797–803. doi:10.2514/3.6278

[5] Pate, S. R., "Measurements and Correlations of Transition Reynolds Numbers on Sharp Slender Cones at High Speeds," *AIAA Journal*, Vol. 9, No. 6, June 1971, pp. 1082–1090. doi:10.2514/3.49919

[6] Dougherty, N. S., Jr., "Correlation of Transition Reynolds Number with Aerodynamic Noise Levels in a Wind Tunnel at Mach Numbers 2.0–3.0," *AIAA Journal*, Vol. 13, No. 12, Dec. 1975, pp. 1670–1671. doi:10.2514/3.7045

[7] Dougherty, N. S., Jr., and Fisher, D. F., "Boundary-Layer Transition on a 10-Degree Cone: Wind Tunnel/Flight Correlation," AIAA Paper 80-0154, Jan. 1980.

[8] Pate, S. R., "Effects of Wind Tunnel Disturbances on Boundary-Layer Transition with Emphasis on Radiated Noise: A Review," AIAA Paper 80-0431, March 1980.

[9] Pate, S. R., "Dominance of Noise on Boundary Layer Transition in Conventional Wind Tunnels—A Place for the Quiet Ballistic Range in Future Studies," *Instability and Transition*, edited by M. Y. Hussaini and R. G. Voight, Vol. 1, Springer–Verlag, New York, 1990, pp. 77–87.

[10] Reshotko, E., "A Program for Transition Research," *AIAA Journal*, Vol. 13, No. 3, March 1975, pp. 261–265. doi:10.2514/3.49690

[11] Schneider, S. P., "Effects of High-Speed Tunnel Noise on Laminar-Turbulent Transition," *Journal of Spacecraft and Rockets*, Vol. 38, No. 3, May–June 2001, pp. 323–333. doi:10.2514/2.3705

[12] Sheetz, N. W., Jr., "Free-Flight Boundary Layer Transition Investigations at Hypersonic Speeds," AIAA Paper 65-127, Jan. 1965.

[13] Sheetz, N. W., Jr., "Boundary-Layer Transition on Cones at Hypersonic Speeds," AIAA Paper 67-131, Jan. 1967.

[14] Sheetz, N. W., Jr., "Ballistics Range Boundary-Layer Transition Measurements on Cones at Hypersonic Speeds," *Symposium on Viscous Drag Reduction*, Plenum Press, New York, 1969, pp. 53–83.

[15] Potter, J. L., "Observations on the Influence of Ambient Pressure on Boundary-Layer Transition," *AIAA Journal*, Vol. 6, No. 10, Oct. 1968, pp. 1907–1911. doi:10.2514/3.4899

[16] Potter, J. L., "Boundary-Layer Transition on Supersonic Cones in an Aeroballistic Range," *AIAA Journal*, Vol. 13, No. 3, March 1975, pp. 270–277. doi:10.2514/3.49692

[17] Reda, D. C., "Boundary-Layer Transition Experiments on Sharp Slender Cones in Supersonic Free Flight," *AIAA Journal*, Vol. 17, No. 8, Aug. 1979, pp. 803–810. doi:10.2514/3.61231

[18] Reda, D. C., and Raper, R. M., "Measurements of Transition-Front Asymmetries on Ablating Graphite Nosetips in Hypersonic Flight," *AIAA Journal*, Vol. 17, No. 11, Nov. 1979, pp. 1201–1207. doi:10.2514/3.61301

[19] Reda, D. C., Wilder, M. C., Bogdanoff, D. W., and Prabhu, D. K., "Transition Experiments on Blunt Bodies with Distributed Roughness in Hypersonic Free Flight," *Journal of Spacecraft and Rockets*, Vol. 45, No. 2, March–April 2008, pp. 210–215. doi:10.2514/1.30288

[20] Reda, D. C., Wilder, M. C., and Prabhu, D. K., "Transition Experiments on Blunt Bodies with Isolated Roughness Elements in Hypersonic Flight," *Journal of Spacecraft and Rockets*, Vol. 47, No. 5, Sept.–Oct. 2010, pp. 828–835. doi:10.2514/1.49112

[21] Reda, D. C., "Review and Synthesis of Roughness-Dominated Transition Correlations for Reentry Applications," *Journal of Spacecraft and Rockets*, Vol. 39, No. 2, March–April 2002, pp. 161–167. doi:10.2514/2.3803

[22] Schiller, L., "Flow in Pipes," *Handbook of Experimental Physics*, Vol. 4, Pt. 4, Academic Press, Leipzig, Germany, 1932, pp. 189–192.

[23] Reshotko, E., and Tumin, A., "Role of Transient Growth in Roughness-Induced Transition," *AIAA Journal*, Vol. 42, No. 4, April 2004, pp. 766–770. doi:10.2514/1.9558

[24] Schneider, S. P., "Effects of Roughness on Hypersonic Boundary-Layer Transition," *Journal of Spacecraft and Rockets*, Vol. 45, No. 2, March–April 2008, pp. 193–209. doi:10.2514/1.29713

[25] Wright, M. J., Candler, G. V., and Bose, D., "Data-Parallel Line Relaxation Method for the Navier–Stokes Equations," *AIAA Journal*, Vol. 36, No. 9, 1998, pp. 1603–1609. doi:10.2514/2.586

[26] Wright, M. J., White, T., and Mangini, N., "Data Parallel Line Relaxation (DPLR) Code User Manual, Acadia-Version 4.01.1," NASA TM-2009-215388, Oct. 2009.

[27] Gordon, S., and McBride, B. J., "Computer Program for Calculation of Complex Chemical Equilibrium Compositions and Applications, I: Analysis," NASA RP-1311, Oct. 1994.

[28] Hill, P. R., Adamson, D., Foland, D. H., and Bressette, W. E., "High-Temperature Oxidation and Ignition of Metals," NACA RM-L55L23b, March 26, 1956.

[29] Touloukian, Y. S., (series editor), *Thermophysical Properties of Matter*, Purdue University, Thermophysical Properties Research Center, New York, IFI/Plenum, 1970-[79], pp. 1434–1463.

[30] Touloukian, Y. S., "Recommended Values of the Thermophysical Properties of Eight Alloys, Major Constituents and Their Oxides," NASA CR-71699, Feb. 1966.

[31] Mell, B., "Topography and Roughness Testing of Sandpaper Surface," NANOVEA Technologies Application Note, http://www.nanovea.com/Application%20Notes/SandPaper.pdf [retrieved 16 May 2011].

[32] Reda, D. C., Wilder, M. C., Bogdanoff, D. W., and Olejniczak, J., "Aerothermodynamic Testing of Ablative Reentry Vehicle Nosetip Materials in Hypersonic Ballistic-Range Environments," AIAA Paper 2004-6829, Nov. 2004.

[33] Wilder, M. C., Reda, D. C., Bogdanoff, D. W., and Prabhu, D. K., "Free-Flight Measurements of Convective Heat Transfer in Hypersonic Ballistic-Range Environments," AIAA Paper 2007-4404, June 2007.

[34] Reda, D. C., Wilder, M. C., and Prabhu, D. K., "Transition Experiments on Slightly Blunted Cones with Distributed Roughness in Hypersonic Flight," AIAA Paper 2011-3417, June 2011.

M. Choudhari
Associate Editor